IEEE Access
Multidisciplinary ⋮ Rapid Review ⋮ Open Access Journal

Received April 11, 2020, accepted April 25, 2020, date of publication April 28, 2020, date of current version May 12, 2020.

Digital Object Identifier 10.1109/ACCESS.2020.2991092

Design of 3D-Printed Flexible Joints With Presettable Stiffness for Surgical Robots

FAN FENG[1], WUZHOU HONG[1], AND LE XIE[1,2], (Member, IEEE)
[1]Institute of Forming Technology and Equipment, Shanghai Jiao Tong University, Shanghai 200030, China
[2]Institute of Medical Robotics, Shanghai Jiao Tong University, Shanghai 200240, China

Corresponding author: Le Xie (lexie@sjtu.edu.cn)

This work was supported in part by the National Natural Science Foundation of China under Grant 61672341, Grant 61973221, and Grant 51911540479, in part by the Project of Science and Technology Commission of Shanghai Municipality under Grant 17441903800, in part by the Guided Key Projects of Science and Technology Plan of Fujian Province under Grant 2018H0032, in part by the Science and Technology Plan project of Quanzhou City under Grant 2018Z028, in part by the Interdisciplinary Program of Shanghai Jiaotong University under Grant YG2017ZD03 and Grant YG2017MS27, and in part by the National Key Research and Development Project under Grant 2017YFB1302900.

ABSTRACT Continuum manipulators have been widely used in minimally invasive surgery due to their high dexterity. However, different surgeries have different stiffness and dexterity requirements. This paper describes a continuum manipulator for robot-assisted surgery. The flexible part is a joint that can be 3D-printed using various materials. The flexible joints made of each material are of the same size but have different stiffness and dexterity. In this way, the appropriate stiffness can be preset by selecting a suitable manufacturing material according to specific surgical needs. Kinematic and static models of the proposed flexible joints were designed. A finite element analysis method was used to calculate the correction factors. We analyzed the workspace and stiffness differences between flexible joints made of different materials quantitatively and qualitatively, respectively. We conducted experiments to verify the accuracy of the static model and the stiffness differences between the flexible joints. Finally, several design variations were introduced, which demonstrate the unique advantages of these flexible joints in the field of surgical robotics.

INDEX TERMS Continuum manipulators, medical robotics, parametric modeling, robot kinematics, design for manufacture.

I. INTRODUCTION

Robot-assisted surgery has attracted increasing attention in recent years, and the advent of flexible continuum manipulators has further expanded the scope of application of minimally invasive robots in clinical surgery [1]. Compared with traditional rigid manipulators or surgical instruments, flexible continuum manipulators that can bend and integrate many types of end effectors or endoscopes improve dexterity and the surgical range of motion [2], [3], whether in natural orifice transluminal endoscopic surgery (e.g., to the skull base [4], maxillary sinus [5], throat [6], and Nissen fundoplication [2]) or in single-port laparoscopic surgery [7], [8]. Robots with variable [9] or controllable stiffness [10], [11], have also drawn a great deal of attention, as they improve the stability of interaction with the human body. Generally, an increase in the dexterity of a continuum manipulator causes a loss of stiffness and force capability [12]. For a surgical continuum robot, it is necessary to possess adequate stiffness to hold payloads during surgery while at the same time having sufficient dexterity to pass through tortuous paths and to be operated in a confined space [13]. Therefore, it is particularly important to balance the relationship between dexterity and stiffness for different minimally invasive surgeries.

Various studies have been conducted on the mechanical structure of flexible continuum manipulators. Typical ones include a cable-driven and a concentric tube mechanism [14]. For a concentric tube manipulator, Sears and Dupont [15] designed a steerable needle based on sets of curved concentric tubes, which performs surgical operations on sensitive tissue and body cavities. Burgner *et al.* [16] designed a similar structure with an outer diameter of only 3.05 mm, which performs transnasal skull base operations. The motion of this kind of continuum robots is achieved by a combination of rolling and sliding but without bending, which limits their dexterity and controllable snapping [17], presenting a degree of difficulty

The associate editor coordinating the review of this manuscript and approving it for publication was Chenguang Yang.

in narrow surgical path planning. Considering factors such as surgical safety and response speed, cable-driven mechanisms are the most prominent candidate for surgical robots [18]. Therefore, this article focuses on the cable-driven continuum manipulator, which can be classified according to whether or not its bending is achieved by elastic deformation [19].

One type of cable-driven continuum manipulator is a structure in which multiple small joints are connected by cables. Hong *et al.* [5] designed a continuum manipulator for wide-angle bending by pulling multiple stainless steel joints connected in a series for maxillary sinus surgery. Kim *et al.* [11] designed a 2-module 4-DOF manipulator with a series of links. Each link has two cylindrical contact surfaces, oriented orthogonally to each other to achieve bending. The link, whose outer diameter is 20 mm, is mainly made using 3D fused deposition manufacturing. Another type is a structure that relies on elastic deformation of the joints to produce bending. Yoon and Yi [20] and Kanno *et al.* [21] developed two similar 4-DOF bending mechanisms with two joints. Each joint consists of a backbone and a series of supporting collars with cables passing through. Haraguchi *et al.* [22] designed a spring-like machined structure. Its end stiffness is about 0.71 N/mm, and its outer diameter is 10 mm. Hu *et al.* [23] designed and manufactured a 3D-printed helical-structured flexible joint with a diameter of 9 mm using selective laser melting (SLM), but with a single joint having only one bending degree of freedom (DOF) to prevent undesirable axial compression. It is made exclusively of 316L stainless steel.

Due to the effect of non-linear friction, the bending angles of different joints of the first type are usually significantly different [5], [24]. The second type usually produces a smoother body shape [23], which is helpful for kinematic modeling. However, the current processing method of the second type is mainly mechanical. If the manufacturer wants to obtain a smaller diameter, this adds further requirements to the manufacturing process, which also means an increase in cost. Nowadays, using metal 3D printing technology can shorten the technological process while reducing the fabrication cost.

At present, most of the stiffness control for flexible continuum manipulators is achieved by changing the designed flexible structure's geometric or material properties [25]. A typical method is to use a outer sheath with fixed stiffness or to control its stiffness by, for example, memory alloys or magnetic fluids. Then, by controlling the position [26] or stiffness of the sheath [27], the continuum manipulator's stiffness can be changed. Instead of adding structure on the outside of continuum manipulator, Brancadoro *et al.* [28] designed a novel kind of stiffening system based on fiber jamming transition that can be embedded in the channels of manipulator. Shiva *et al.* [29] also developed a pneumatically actuated soft manipulator with tendons incorporated in the structure complement the pneumatic actuation placed inside the manipulator's wall to adjust overall stiffness. However, applying a sheath or adding a stiffness control channel in a continuum manipulator will necessarily increase the dimensions. In addition to those, the solution based on granular jamming [30], [31] also has the same disadvantage of increasing dimensions. For minimally invasive surgery with strict size requirements, such as natural human cavity surgery (e.g., to the maxillary sinus), an increase in size is unacceptable. In this respect, Kim *et al.* [11] presents a hyperredundant tubular manipulator with a variable neutral-line mechanisms to achieve adjustable stiffness. The basic mechanics of variable neutral-line manipulator with stiffness characteristics can be manufactured according to the stiffness requirements of a specific minimally invasive surgery. In this way, the problem of increasing the dimensions can be solved by presetting the stiffness of continuum manipulator in manufacture phase rather than during the surgery. However, their method is only applicable to a continuum manipulator with multi-sections structure but not the bending joints that rely on elastic deformation.

Moreover, stiffness control of flexible continuum manipulators based on kinematics and statics model [10] or the force feedback of continuum manipulators [32], [33] also attracted a lot of attention in this field. Whether from the perspective of precise control or potential development value, it is an indispensable part to establish the kinematics and statics model of the designed continuum manipulator.

Therefore, this paper proposes a helical spring-like flexible joint that can be manufactured using 3D printing technology. The flexible joint relies on elastic deformation to produce a smoother bending shape. What is more, it can be 3D-printed using a variety of materials, including metals and non-metals. So it brings more benefits such as the flexible joints can be preset or combined, with different degrees of stiffness and dexterity. Section II details the kinematic and static models of this flexible joint and the parameters modified in a finite element analysis. The differences in workspace and stiffness between flexible joints made of different materials are analyzed quantitatively and qualitatively, respectively. Section III presents the design of a static model validation system to verify the accuracy of the static model and a stiffness experiment to evaluate the stiffness differences between metallic flexible joints. Moreover, some design variations are introduced and the benefits of our work for surgical robot applications are summarized. Section IV concludes and presents our directions of future work based on this paper.

II. DESIGN AND MODELING OF THE FLEXIBLE JOINT

A. DESIGN AND FABRICATION

Fig. 1 presents an overview of a master-slave flexible surgical robot system that can be used for robot-assisted laryngeal biopsy. The system consists of four parts: the continuum manipulator system, a 6-DOF manipulator (UR5e), a PC, and a remote operation controller (Geomagic Touch). The continuum manipulator has a 2-DOF bending function with a 2.3-mm instrument channel. It can be inserted into a biopsy forceps or radiofrequency ablation equipment for laryngeal surgery, or it can be inserted into an endoscope for

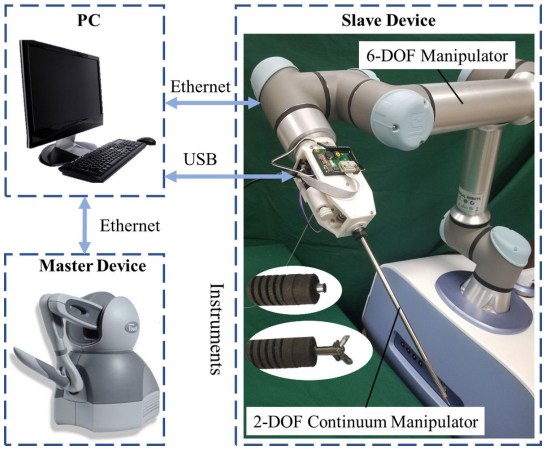

FIGURE 1. Overview of the flexible surgical robot system.

observation. The continuum manipulator system is mounted on a 6-DOF manipulator to perform the spatial positioning function. These two parts constitute the slave device of the entire system. The continuum manipulator system is connected to the PC through a USB interface, and the 6-DOF manipulator and the master controller are connected to the PC through Ethernet cables. The position and pose of the master controller are mapped to the slave device consisting of the continuum manipulator system and the 6-DOF manipulator to perform point-to-point positioning control.

This article focuses on the analysis and modeling of the flexible joint, an important part of the continuum manipulator system. Fig. 2 is a schematic of the designed spring-like flexible joint. Its structure is divided into three main parts. The first is a rigid distal functional part that can be integrated with surgical instruments. The second part is a helical structure that provides bending deformation. The spring structure includes four circular threading holes. The centres of the threading holes are located at the middle diameter of the helical structure. The cables can pass through the entire flexible part through those holes. The third part is an assembly part, which is convenient for connecting the control mechanism.

This article focuses on the analysis and modeling of the flexible joint, an important part of the continuum manipulator system. Fig. 2 is a schematic of the designed spring-like flexible joint. Its structure is divided into three main parts. The first is a rigid distal functional part that can be integrated with surgical instruments. The second part is a helical structure that provides bending deformation. The spring structure includes four circular threading holes. The centres of the threading holes are located at the middle diameter of the helical structure. The cables can pass through the entire flexible part through those holes. The third part is an assembly part, which is convenient for connecting the control mechanism.

Compared with other flexible joints structures, this type of structure has the following advantages:

1) The structures are 3D printable with various materials to preset the stiffness and dexterity according to the requirements of different minimally invasive surgeries.

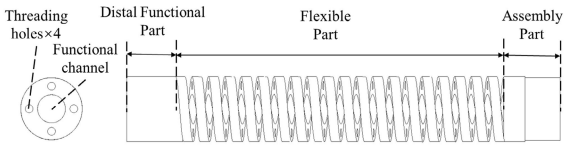

FIGURE 2. Side view and front view of spring-like flexible joint.

2) 3D printing technology reduces processing steps and manufacturing costs [23].
3) Compared with structures using a spring as a backbone [20], the control cable directly passes through the flexible part, which reduces the control spacing and the model's margin of error.
4) It allows for highly customizable sizes and assembly designs for different types of surgical instruments.

In this study, flexible joints were manufactured using SLM technology. They can be made from a range of metal powders, including titanium alloy TC4 (Ti–6Al–4V), maraging steel 18Ni300, stainless steel 316L, etc. In order to improve or control the mechanical properties of flexible joints made of certain materials, different kinds of heat treatment can be performed [34] to meet the requirements for use. In the printing process of the helical structure used in this study, no support structures were added, as deformation without a support structure is minimal for models with small channel sizes [23].

B. KINEMATIC AND STATIC MODELS

The symbols used in the modeling are listed in Table 1.

Consider the following assumptions in the modeling process:

1) As cables with smooth surfaces are used, it can be assumed that the effect of friction between the cables and the threading holes is negligible.
2) The gravity of the flexible joint is much weaker than the external force and can thus be ignored.
3) The pulling force at the knot can be analyzed into pure bending moment and axial force, and in the elastic deformation range, the final deformation can be approximated as a simple superposition of the deformation under those two loads.

As shown in Fig. 3, the cables driven by the servo motor can apply a pulling force at the distal end of the flexible joint. The pulling force at the knot can be analyzed into pure bending moment M and axial force F at the center line of the flexible joint. It can be approximately considered that the superposition of bending deformation and axial compression deformation caused by M and F is the final deformation of the flexible joint [35]. According to the geometric relationship, the rotation angle of the flexible joint can be calculated by the cables' displacement.

$$\theta = \frac{2\Delta L}{D} \tag{1}$$

If we ignore the axial compression deformation, the bending radius of the flexible joint can also be obtained

TABLE 1. Symbols used in the modeling.

Symbols	Description
D_o, D_I, D	Outer, Inner, and Mean coil diameter (mm)
d_o	Threading hole diameter (mm)
θ	Flexible joint bending angle (rad)
β	Angle between bending plane and x-o-z plane (rad)
ΔL	Cable pulling length (mm)
θ_{max}	Maximum bending angle (rad)
l_0	Length of flexible part (mm)
p	Pitch of flexible part (mm)
r	Flexible joint bending radius (mm)
a, b	Cross-section width and height(mm)
φ, γ	Moment-rotation and torsional angle (rad)
A	Sectional area of rectangular spring wire (mm^2)
F	Total axial load on flexible joints (N)
F_x, F_y	Tendon pulling force in threading holes (N)
F_{xy}	Equivalent bending force of F_x and F_y (N)
M	Equivalent bending moment (N·mm)
α	Angle with the initial integral section (rad)
$M(\alpha)$	Bending moment in the cross-section (N·mm)
$T(\alpha)$	Torsion in the cross-section (N·mm)
N	Number of active rings of the helical structure
l	Total coil length along the mean coil (mm)
E, G	Modulus and Shear modulus of elasticity (Mpa)
υ	Poison's ratio
I	Second moment of the area respectively (mm^4)
K	Polar moment of the area respectively (mm^4)
ζ	Angle of hollow circle sector (rad)
U	Strain energy (J)
y	Total axial deflection (mm)
λ_i	Compensation factor of i $(i = I, K, A, \theta, y)$

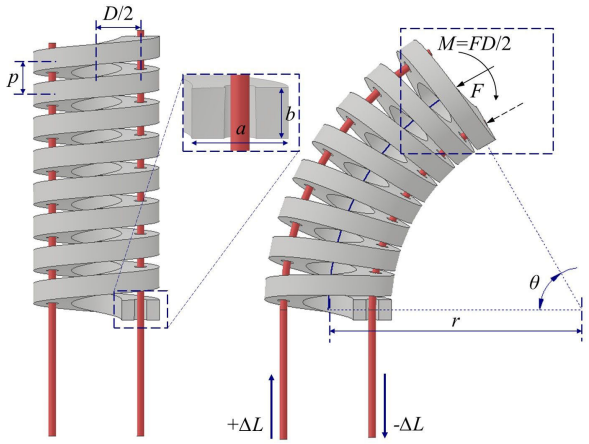

FIGURE 3. Schematic of the bending flexible joint.

geometrically.

$$r = \frac{l_0}{\theta} = \frac{l_0 D}{2\Delta L} \tag{2}$$

If the maximum bending angle $\theta_{\max}$ is reached when the gap between each screw stroke at the edge is zero, the maximum bending angle can be known geometrically.

$$\theta_{\max} = \frac{2Np}{D_O} \tag{3}$$

The kinematic equation is very simple in form, and it is easy to find the position and pose of the flexible joint. For a metallic material with a high elastic modulus and a small degree of bending, the equation can be applied with a small margin of error. However, if it is a non-metal or metal with

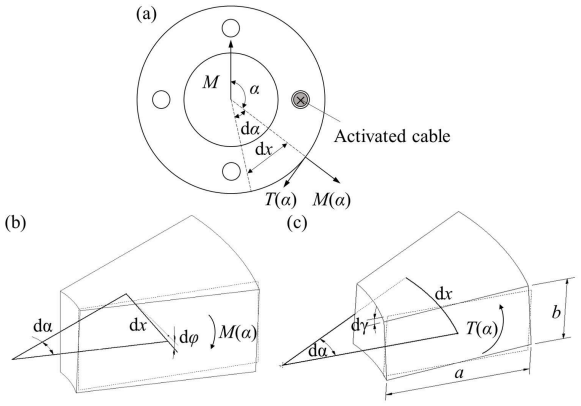

FIGURE 4. Analysis diagram of bending moment and section force.

a low elastic modulus, the effect of axial deformation will be more significant when an axial force is applied, and the equation will result in a greater error. In addition, as the force-position characteristics of different materials are also different, the degree of that influence is also different, so it is necessary to establish a static model. The static modeling method of the flexible joint of this structure is presented below.

As shown in Fig. 4(a), the right hole has a pulling force in an inward direction. In the helical structure, consider an infinitesimal element with an angle range of dα for analysis. The corresponding arc length on the mean coil is dx. Moment M generates bending moment $M(\alpha)$ and torsional moment $T(\alpha)$ on the cross-section, as shown in Fig. 4(b) and 4(c). Consider the role of each of them in the element. Equation (4) presents the internal and external work of loads.

$$\frac{1}{2}M\theta = \frac{1}{2}\int M(\alpha)d\varphi + \frac{1}{2}\int T(\alpha)d\gamma \tag{4}$$

where dφ is the bending moment angle on the element, and dγ is the twist angle.

The bending angle that can be generated under the action of the bending moment $M(\alpha)$ can be expressed as (5).

$$d\varphi = \frac{M(\alpha)}{EI}dx \tag{5}$$

For rectangular sections, $I = ab^3/12$. Knowing from the geometric relationship that $D\mathrm{d}\alpha = 2\mathrm{d}x$, if the number of active rings of the flexible joint is N, then

$$\int M(\alpha)d\varphi = \int_0^{2\pi N} \frac{DM(\alpha)^2}{2EI}d\alpha = \frac{\pi N F^2 D^3}{8EI}. \tag{6}$$

Unlike the spring with a circular cross-section, the torsional moment is more complicated in a rectangular cross-section. Some scholars have performed theoretical analyses for the calculation of the deformation and stress in a rectangular cross-section through the principle of elasticity [36], [37]. In this study, the algorithm in [37] was adopted, that is, the torsional angle that can be generated under the action of

torque is

$$d\gamma = \frac{T(\alpha)}{GK}dx. \tag{7}$$

Therefore,

$$\int T(\alpha)d\gamma = \int_0^{2\pi N} \frac{T(\alpha)^2 D}{2GK}d\alpha = \frac{\pi N F^2 D^3}{8GK} \tag{8}$$

$$K = \frac{ab^3}{8}\left[\frac{16}{3} - 3.36\frac{b}{a}\left(1 - \frac{b^4}{12a^4}\right)\right] \tag{9}$$

Thus, the bending angle can be calculated by (10).

$$\theta = \frac{\pi N F D^2}{4}\left(\frac{1}{EI} + \frac{1}{GK}\right) \tag{10}$$

However, the above deduction process is conditioned on the absence of cracks in the rectangular cross-section. The designed flexible joint has some rectangular cracks in its section due to the existence of the threading holes through which the cable passes. This is bound to cause errors [38]. Therefore, it is necessary to add the structural correction factors λ_I and λ_K, which are related to I and K, respectively. If the material and size of the flexible joint are determined, EI and GK are both constant. The correction factors can be simplified to one λ_θ, and (10) can be rewritten as

$$\theta = \frac{\pi N F D^2}{4}\left(\frac{\lambda_I}{EI} + \frac{\lambda_K}{GK}\right) = \frac{\pi \lambda_\theta N F D^2}{4}\left(\frac{1}{EI} + \frac{1}{GK}\right). \tag{11}$$

The force F acting on the centerline of the flexible joint will cause compression, which in turn will cause the bending radius to change. From the geometric relationship, the bending radius of the helical structure r under the action of F is calculated as

$$r = (l_0 - y)/\theta. \tag{12}$$

where y is the axial deformation of the flexible joint, and l0 is the original length of the flexible part. The specific deducing steps are given below, analogous to the modeling method of circular cross-section springs [39].

Under the action of axial load F, the strain energy U of the helical structure can be expressed as

$$U = \frac{T^2 l}{2GK} + \frac{F^2 l}{2AG} = \frac{\pi \lambda_K N F^2 D^3}{8GK} + \frac{\pi \lambda_A N F^2 D}{2AG}. \tag{13}$$

where $T = FD/2$ is the torque on the rectangular section, $A = ab$ is the rectangular cross-sectional area, and $l = \pi DN$ is the total coil length. Then, the axial deformation y can be calculated using Castigliano's theorem.

$$y = \frac{\partial U}{\partial F} = \pi \lambda_y N F D\left(\frac{D^2}{4GK} + \frac{1}{AG}\right) \tag{14}$$

where λ_A is the correction factor related to A, and λ_y is the overall correction factor. By substituting (12) for (14), the bending radius can be obtained. The above analysis also shows that the bending angle and axial compression of the flexible joint are independent of the pitch of the flexible structure and only affect the maximum bending angle and the maximum axial compression.

TABLE 2. The mechanical parameters used in FEA.

Material	Elastic Modulus (Gpa)	Shear Modulus (Gpa)	Yield Strength (Mpa)
316L (Stainless Steel)	197.0	75.8	550 ± 50
18Ni300 (Maraging Steel)	160.0	61.5	1050 ± 100
18Ni300 (heat-treated[a])	170.0	65.4	1900 ± 100
AlSi10Mg (Aluminum)	64.0	24.1	270 ± 30
TC4 (Titanium)	129.0	49.2	1000 ± 50
In718 (Inconel)	186.0	72.4	800 ± 70
In718 (heat-treated[b])	195.0	75.9	1350 ± 100
CoCrMo (Cobalt Chrome)	222.0	84.6	900 ± 100

[a] Aging temperature 490 °C (914 °F), 6 hours, air cooling.
[b] First, solution treated at 980 ± 10 °C for 1 hour. Then, aged at 720 ± 10 °C for 8 hours, and finally aged at 620 ± 10 °C for 8 hours.

C. MODEL CORRECTION BASED ON FINITE ELEMENT ANALYSIS

In order to calculate the correction factors λ_θ and λ_y, which are difficult to obtain in the theoretical static model, and also to prevent some parts of the joint from entering a plastic deformation phase due to the excessive bending angle during the experiment. In this study, static analysis was performed using Abaqus Standard solver. The specific dimensions are 5 mm in outer diameter, 1.2 mm in inner diameter, 1.4 mm in pitch, 30 active rings, and 43.15 mm in total length of the flexible part with flat ends. In the finite element analysis (FEA), the material properties were set to linear elastic materials. The mechanical parameters used in FEA, tested using standard American Society for Testing and Materials (ASTM) E8 methods, are shown in Table 2.

Fig. 5 shows the finite element analysis simulation result of the flexible joint made of 18Ni300 when the tensile force is 38.7 N. It can be seen that under the action of bending moment or axial concentrated force, the stress distribution is relatively uniform, and the rotation angle and compression of each helical turn structure are approximately the same. Thus, the bending curvature is also relatively uniform. At the same time, it can be observed that under the action of the bending moment, the area near the threading holes at 90° adjacent to the activated cable has the maximum Von Mises stress. Under the concentrated pressure load, the maximum Von Mises stress locations are distributed at the inner wall of the helical structure. It has also been found in experiments that this is the point of crack initiation. In this case, it is possible to optimize the structure of flexible joints using finite element analysis, which has been extensively studied [40], [41].

During static loading process, the external force increases linearly with time. Regards to this, we use n_1 and n_2 shown in the Fig. 5 as the monitored nodes, and record the coordinate information of $n_1, n_2 \in \mathbb{R}^2$ at each output step. In this way, the bending angle θ and the axial deformation y at time t can be obtained by (15). Meanwhile, the value of maximum Von Mises stress is also monitored. The FEA process will stop when this output value is greater than the yield strength of

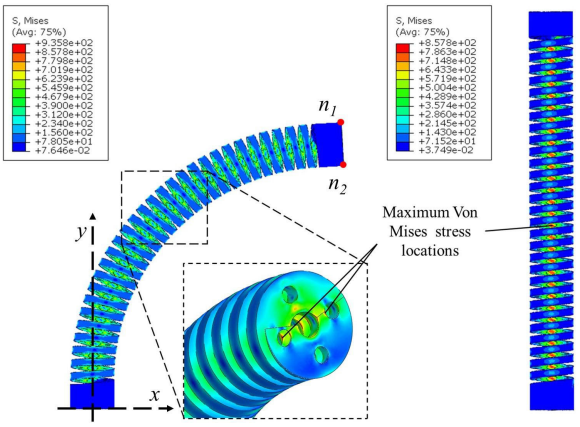

FIGURE 5. FEA result of the 18Ni300 flexible joint with a 38.7N pulling force.

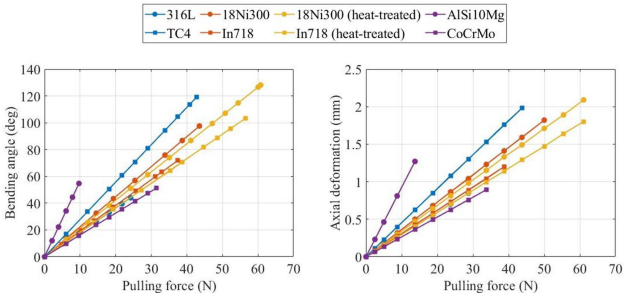

FIGURE 6. Finite element analysis data.

TABLE 3. Correction factors based on finite element analysis.

Material	λ_θ	λ_y
316L (Stainless Steel)	1.279	1.063
18Ni300 (Maraging Steel)	1.280	1.065
18Ni300 (heat-treated)	1.280	1.065
AlSi10Mg (Aluminum)	1.282	1.060
TC4 (Titanium)	1.280	1.061
In718 (Inconel)	1.278	1.067
In718 (heat-treated)	1.279	1.067
CoCrMo (Cobalt Chrome)	1.280	1.065

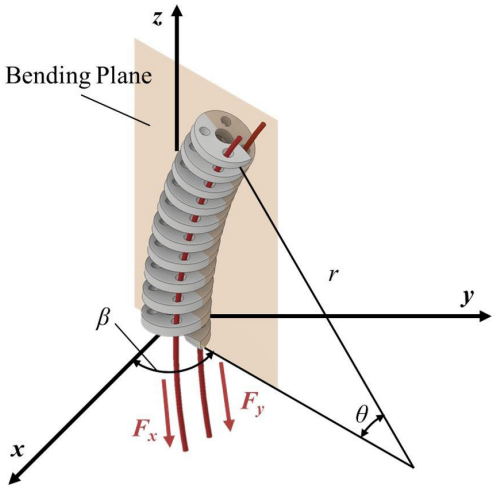

FIGURE 7. Schematic of the flexible joint bending in three-dimensional space.

the material.

$$\theta(t) = \left\langle (1,0), \overrightarrow{n_1(t)n_2(t)} \right\rangle$$
$$y(t) = \frac{1}{2} \|n_1(t) + n_2(t) - n_1(0) - n_2(0)\| \quad (15)$$

As shown in Fig. 6, the bending angle of different materials under M and the axial compression under F are verified by the finite element method. It can be observed that, corresponding to the static model, the bending angle and the axial compression are proportional to the tension, and the higher the elastic modulus of the material, the smaller of the slope. It can also be seen in Table 2 and Fig. 6 that the TC4 titanium alloy flexible joint of this structure can produce a large deflection angle θ with less bending moment. This means that the tension requirement of the pulling cable is smaller, which reduces not only the strength requirement of the driven cables but also the output torque that the servo motor should provide. For a flexible joint made of AlSi10Mg, the tensile force required and the stiffness are weaker when it undergoes great deformation, but it may enter the plastic deformation phase prematurely, which affects the repeated use of the flexible joint or results in fracture, causing safety issues. In short, in theory, the more easily the material deforms, the less stiffness the flexible joint made of it has. If the length of the flexible joint is the same, the deflection angle that can be used in the safe range is also affected by the yield stress of the material.

From Fig. 6, (11), and (14), it can be known that within the elastic deformation, the deflection angle and compression of the flexible joint are proportional to the applied tension. The difference is that because the theoretical model uses the method of modifying coefficients to modify the section coefficients, whereas the finite element method directly considers the effect of section changes in the model, the results calculated by the finite element method should be closer to the real conditions. The results obtained from the finite element analysis can be used to calculate the correction factors in the theoretical static model.

Based on the results of the finite element analysis shown in Table 3, we can conclude that the ideal correction factors can be considered as $\lambda_\theta = 1.280$ and $\lambda_y = 1.064$. Compared with no-cracks sections, flexible joints with threading holes should be more prone to deformation. Therefore, the two correction factors greater than 1 are also in accord with objective laws.

D. ANALYSIS OF WORKSPACE AND STIFFNESS

Fig. 7 is a schematic of a flexible joint bending in three-dimensional space. In the initial state, the apex of the flexible joint is located at the origin of the coordinate axis, and its axial direction coincides with the z-axis. Since the flexible joint is bent, only one of the two driven cables on the opposite corners is tightened, while the other two are in a relaxed state. Therefore, the pulling force of the cable inside the threading hole located at the x-axis in free state can be defined as F_x. $F_x > 0$ when the threading cable in the positive axis is activated, and $F_x < 0$ when the threading cable in the negative axis is activated. A similar definition applies to F_y.

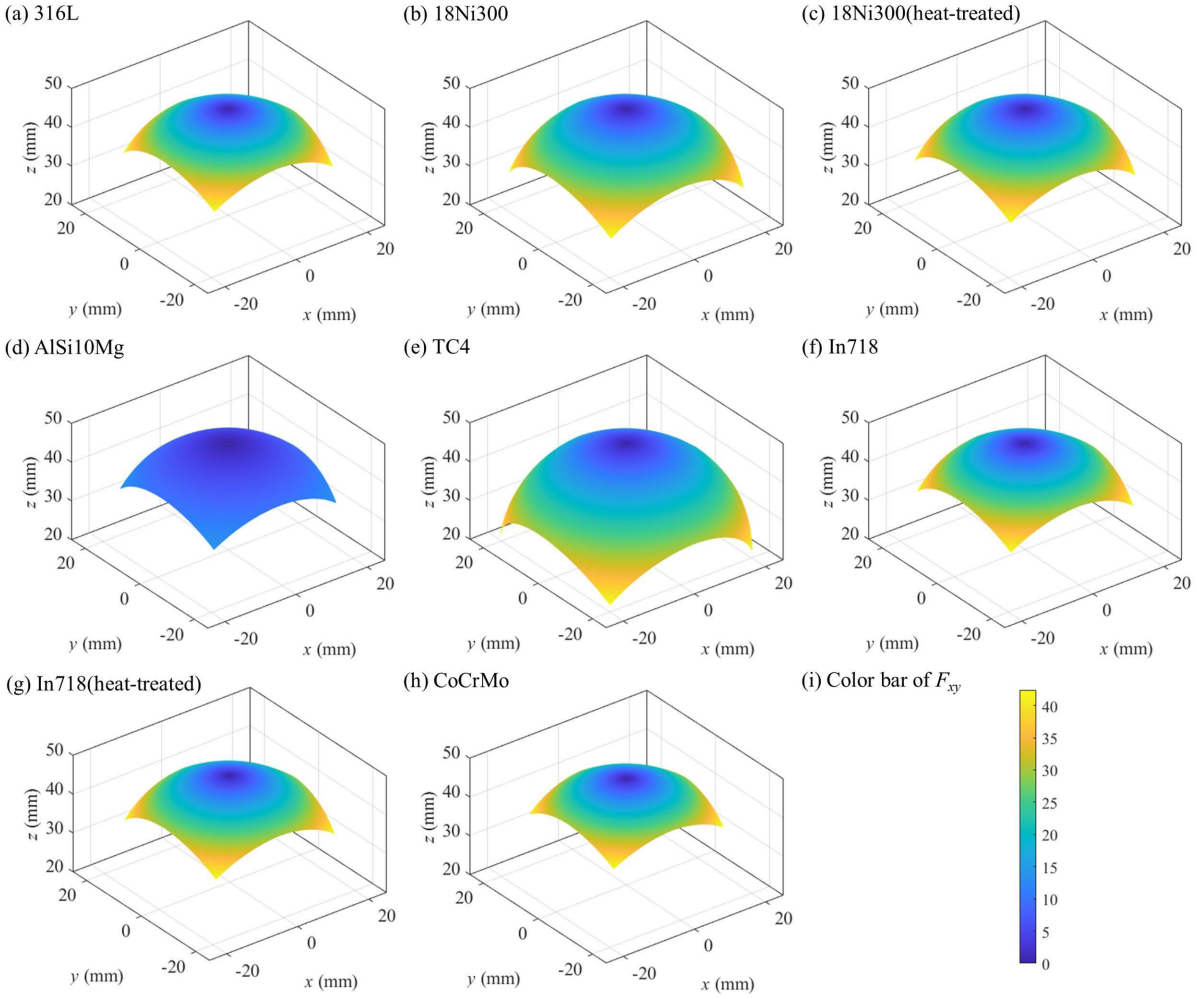

FIGURE 8. Workspace differences in different materials.

The angle between the bending plane and the x-o-z plane is γ. Together with θ and r, the flexible joint's position and pose can be expressed.

The kinematic and static models of unidirectional cable-driven flexible joints have been analyzed above. If the basic assumption holds, it is also applicable to three-dimensional space because the tensile forces F_x and F_y can be analyzed and combined into a total bending moment and axial load.

$$M = \frac{D\sqrt{F_x^2 + F_y^2}}{2} \tag{16}$$

$$F = |F_x| + |F_y| \tag{17}$$

If the equivalent bending force is defined as $F_{xy} = \sqrt{F_x^2 + F_y^2}$, then

$$\theta = \frac{\pi \lambda_\theta N F_{xy} D^2}{4}\left(\frac{1}{EI} + \frac{1}{GK}\right) \tag{18}$$

$$y = \pi \lambda_y N F D\left(\frac{D^2}{4GK} + \frac{1}{AG}\right) \tag{19}$$

β is the angle between the positive unit vector of the x-axis and $(F_x, F_y, 0)$.

$$\beta = \langle (1, 0, 0), (F_x, F_y, 0) \rangle \tag{20}$$

According to the above analysis, the workspaces of flexible joints for different materials with the same size as in the finite element analysis were derived, and the results shown in Fig. 8 were obtained. Of which, $F_x, F_y \in [-30, 30]$ (N). According to the result of FEA, AlSi10Mg will enter the plastic phase prematurely when the pulling force reached 10 N, thus, set its $F_x, F_y \in [-10, 10]$ (N). It can be seen that for a flexible joint made of a material with a higher elastic modulus, the working space is smaller under the same driving force.

Besides the workspace, the stiffness of flexible joints made of different materials must be different. Due to the complexity of the load form and the cross-sectional shape, only the factors that affect the stiffness of this type of flexible joint were analyzed qualitatively.

Analogous to the definition of bending stiffness of simply supported beams, the stiffness of a flexible joint can be

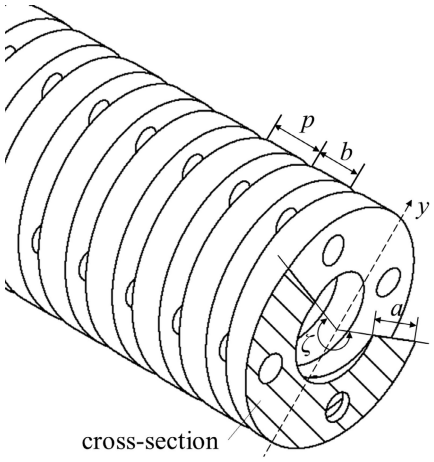

FIGURE 9. Schematic of the hollow circle sector.

defined as EI, where E is the elastic modulus and I is the section moment of inertia [25]. As shown in Fig. 9, because it is a helical structure, its cross-section is not a regular torus but a hollow circle with an angle of ζ.

From the geometric relationship, the angle ζ of the hollow circle can be calculated by (21).

$$\zeta = \frac{2\pi b}{p} \tag{21}$$

According to [31], if the y-axis is the symmetry axis of the hollow circle, the section moment of inertia is

$$\begin{aligned} I_x &= \frac{D_O^3 a}{8} \\ &\times \left[\left(1 - \frac{3a}{D_O} + \frac{4a^2}{D_O^2} - \frac{2a^3}{D_O^3}\right) \left(\frac{\zeta + \sin\zeta}{2} - \frac{2\sin^2\frac{\zeta}{2}}{\varphi}\right) \right. \\ &\left. + \frac{4a^2\sin^2\frac{\zeta}{2}}{3D_O^2\varphi(1 - a/D_O)} \left(1 - \frac{2a}{D_O} + \frac{2a^2}{3D_O^2}\right) \right] - I_{ox} \\ I_y &= \frac{D_O^3 a}{8} \left(1 - \frac{3a}{D_O} + \frac{4a^2}{D_O^2} - \frac{2a^3}{D_O^3}\right) \left(\frac{\zeta - \sin\zeta}{2}\right) - I_{oy} \end{aligned} \tag{22}$$

where I_{ox} and I_{oy} are the cross-section moment of inertia of the threading holes on the x-axis and y-axis, respectively.

From the geometric relationship, it can be seen that I_{ox} and I_{oy} are positively related to the diameter of the threading holes do. It can be known from (22) that I_x and I_y are positively related to the angle ζ, the helical outer diameter D_O, and the section width a.

According to the above analysis, the parameters affecting the stiffness can be obtained (Table 4). Under certain flexible joint material and load conditions, the stiffness of the flexible joint is positively related to its outer diameter D_O, section width a, and section thickness b, but the pitch p and the diameter of the threading hole d_o are negatively related. Under certain structure size and load conditions, the stiffness of the flexible joint is proportional to the elastic modulus of the material used.

TABLE 4. Correction factors based on finite element analysis.

Stiffness Influence Parameter	Positive Correlation	Negative Correlation
I	D_O, a, b	p, d_o
E	Material types and heat treatment conditions	

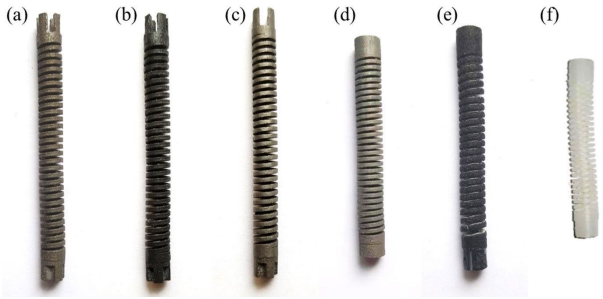

FIGURE 10. Manufactured flexible joints. (a) 18Ni300. (b) 18Ni300 (heat-treated). (c) TC4. (d) 316L. (e) Hard rubber. (f) Soft rubber.

III. EXPERIMENT AND VALIDATION

Because there are errors in the actual manufacturing process of flexible joints, it is not guaranteed that the mechanical properties of all manufactured flexible joints accurately match the statistical averages in Table 2. The above mentioned causes of errors cannot be estimated and calculated in the finite element analysis. Therefore, the finite element analysis only verifies the ideal model, and it should deviate from the actual use process of the flexible joint. In order to further verify the accuracy of the static model and evaluate its performance differences more accurately, it is necessary to perform static and stiffness tests of the flexible joint entity.

A. EXPERIMENTAL MATERIALS AND METHODS

Flexible joints made of several different metals and with the mechanical structure parameters shown in Fig. 10 were selected to verify the accuracy of the static model. The structural dimensions in Fig. 10(a), 10(b), and 10(c) are 5 mm in outer diameter, 1.2 mm in inner diameter, 0.8 mm in threading hole diameter, and 1.4 mm in pitch. The structural dimensions in Fig. 10(d) are 6 mm in outer diameter, 1.2 mm in inner diameter, 0.8 mm in threading hole diameter, and 1.3 mm in pitch. This is because the material used for the flexible joint shown in Fig. 10(d) is 316L, which has a higher value of elasticity modulus and lower yield stress. Therefore, to avoid fracture, a larger outer diameter and smaller pitch are needed.

In addition, as shown in Fig. 10(e) and 10(f), this structure can also be made of non-metals such as hard and soft rubber. Hard rubber can be preset to varying hardness in 3D printing. However, due to the poor rigidity of non-metallic flexible joints, a wide bending angle can be generated by a minute driving force. Compared with the driving force, the effect of their own gravity is greater. Moreover, when

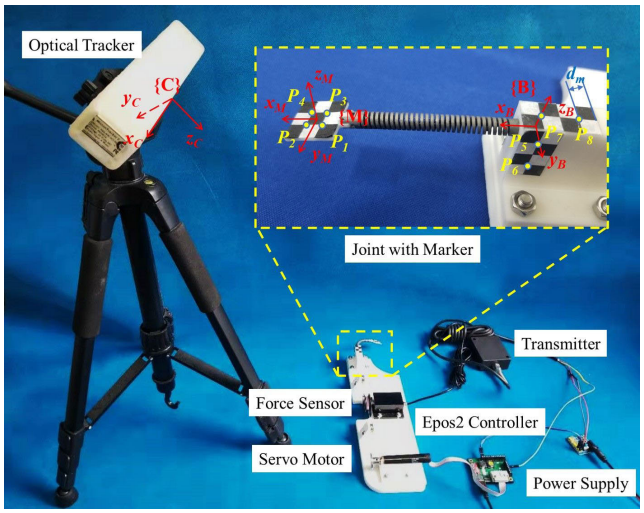

FIGURE 11. Model verification system.

the helical clearance of the flexible joint reaches zero, it can continue to deform even after θ_{max} is reached. For this reason, the verification of its static model is not presented in this section.

An overview of the hardware testing system is shown in Fig. 11. The experiment used the MicronTracker3 optical tracking system and a marker plate to record the position and pose of the flexible joint. The marker plate has four marked points(P_1, P_2, P_3, P_4) to obtain the position and pose information, that is, the coordinate system $\{M\}$. During the test, the coordinate system moves with the marker plate, with its z-axis perpendicular to the joint bending plane at all times. Another six marked points(take four of them P_5, P_6, P_7, P_8 for calculation) on the flexible joint base are used to obtain the base coordinate system orientation of the flexible joint, that is, the coordinate system $\{B\}$. During the test, it has no relative movement to the coordinate system $\{C\}$. So these points(P_5, P_6, P_7, P_8) should be blocked for higher detection accuracy of the points on the marker plate. A Maxon RE 13 motor with a 275:1 reduction ratio planetary gearhead is used to perform displacement operations on the cables passing through the threading holes, which can provide a 0.3 N·m continuous torque. Cables are connected and knotted to both the flexible joint end and the motor output shaft. The side pressure force sensor and pulley are combined to measure the cables' tension. An EPOS2 24/2 Positioning Controller monitors the motor encoder signal in real time, as well as the tension voltage signal with its 12-bit resolution analog signal input port. The entire test system is powered by a 12-V DC power supply. The optical tracking system and the EPOS2 controller are connected to the PC. On the PC, the position of the flexible joint and the displacement and tension data of the cables can be monitored and recorded in real time.

B. VALIDATION OF THE STATIC MODEL

With the testing system shown in Fig. 11, the three-dimensional coordinate values of the marked points can be obtained by the optical tracking system. In order to correspond to the static model, the position information related to $\{M\}$ needs to be expressed in $\{B\}$. To this end, we propose the following calculation steps.

The coordinate values P_i in $\{C\}$ can be represented by column vectors $(x_i, y_i, z_i)^T \in \mathbb{R}^3$, and the unit vectors of the x, y, z axis of coordinate system $\{M\}$ and $\{B\}$ are expressed as $\hat{n}$,$\hat{o}$ and $\hat{a}$ respectively. According to the geometric relationship, the orientation vectors can be obtained by (23).

$$\begin{aligned} \overrightarrow{O_C O_B} &= \overrightarrow{O_C P_7} + \frac{1}{2}\overrightarrow{P_5 P_6} \\ \overrightarrow{O_C O_M} &= \frac{1}{4}\sum_{i=1}^{4}\overrightarrow{O_C P_i} \end{aligned} \tag{23}$$

And the unit vectors of $\{M\}$ and $\{B\}$ can also calculated by (24).

$$\begin{aligned} \widehat{n_M} &= \frac{1}{2}\left(\frac{\overrightarrow{P_1P_2}}{\left|\overrightarrow{P_1P_2}\right|} + \frac{\overrightarrow{P_3P_4}}{\left|\overrightarrow{P_3P_4}\right|}\right) \\ \widehat{o_M} &= \frac{1}{2}\left(\frac{\overrightarrow{P_4P_2}}{\left|\overrightarrow{P_4P_2}\right|} + \frac{\overrightarrow{P_3P_1}}{\left|\overrightarrow{P_3P_1}\right|}\right) \\ \widehat{n_B} &= \frac{\overrightarrow{P_8P_7}}{\left|\overrightarrow{P_8P_7}\right|},\ \widehat{a_B} = \frac{\overrightarrow{P_6P_5}}{\left|\overrightarrow{P_6P_5}\right|} \end{aligned} \tag{24}$$

Thus, the conversion relationship of the coordinate systems $\{C\}$ to $\{B\}$ and $\{C\}$ to $\{M\}$ can be obtained by (25) [42].

$$\begin{aligned} A_B^C &= \begin{pmatrix} \widehat{n_B} & \widehat{n_B}\times\widehat{a_B} & \widehat{a_B} & \overrightarrow{O_C O_B} \\ 0 & 0 & 0 & 1 \end{pmatrix}_{4\times4} \\ A_M^C &= \begin{pmatrix} \widehat{n_M} & \widehat{o_M} & \widehat{n_M}\times\widehat{o_M} & \overrightarrow{O_C O_M} \\ 0 & 0 & 0 & 1 \end{pmatrix}_{4\times4} \end{aligned} \tag{25}$$

In this way, the points' location of the coordinate system $\{M\}$ in the coordinate system $\{B\}$ can be obtained. That means we can know the transformation matrix by (26).

$$T_B^M = A_B^C A_C^M = A_B^C (A_M^C)^{-1} \tag{26}$$

According to the assembly relationship, the coordinate axis z_M is perpendicular to the actual bending plane of the flexible joint at all times. Thus, the distance between the coordinate origin in the coordinate system $\{M\}$, which is the actual endpoint and the ideal bending plane along the z_m direction, can be defined as an error ΔZ. Its average value is $\overline{\Delta Z}$, and the standard deviation is σ_Z. The position of the endpoint O_M is projected onto the ideal bending plane and compared with the position calculated by statics. The experimental results are shown in Fig. 12, where the X direction coincides with the direction of the coordinate axis x_B, and the origin of the coordinate also coincides with O_M.

It can be seen in Fig. 12 that when the deflection angle is smaller, the error of the static model is smaller, and when the deflection angle is larger, the error becomes larger. The main reason for this behavior is that the assumptions in the

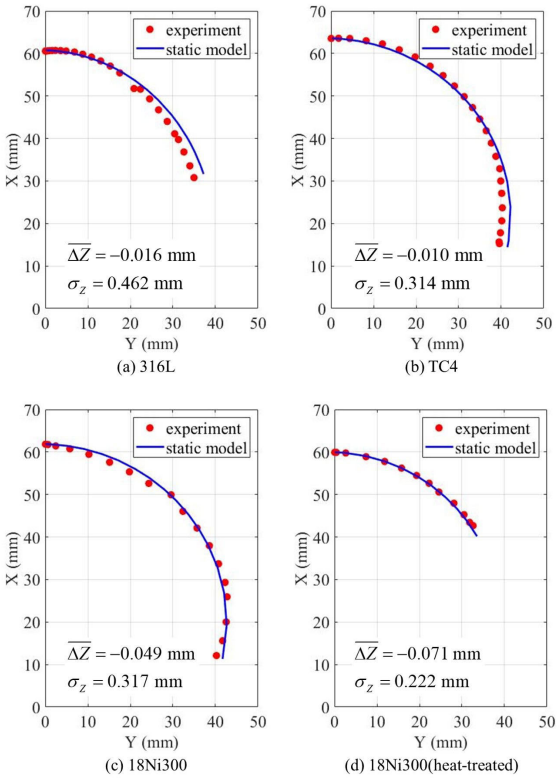

FIGURE 12. Comparison between static model and experiment.

static model differ from the actual conditions. As the tensile force applied by the cables increases, the friction between the cables and the threading holes also gradually increases, and the friction forces are different in different positions, which affects the curvature assumption. For the problem of the small deformation but a large rotating angle, the principle of force superposition is no longer applicable, so the error caused by simply superimposing the deformations caused by bending moment and axial force also increases. What is more, due to the lower yield stress of 316L steel, when the flexible joints made of this material produce a large deflection angle, some areas may have already entered the plastic deformation phase, which may result in a great error. In addition, factors such as the accuracy of the optical tracking system and the force sensor, manufacturing errors in the flexible joint, and the knot state of the cables also affect the experiment's final error.

C. STIFFNESS TEST

In order to evaluate the stiffness differences between flexible joints made of different materials, a series of standard weights can be used to test the stiffness of each. Without a pulling force, some standard weights are hung on the end of the flexible joint, and its deflections in displacement and angle are measured. Fig. 13 shows the condition of the flexible joint made of maraging steel 18Ni300 (heat-treated) during the stiffness test. The optical tracking method is still used to monitor the deflection.

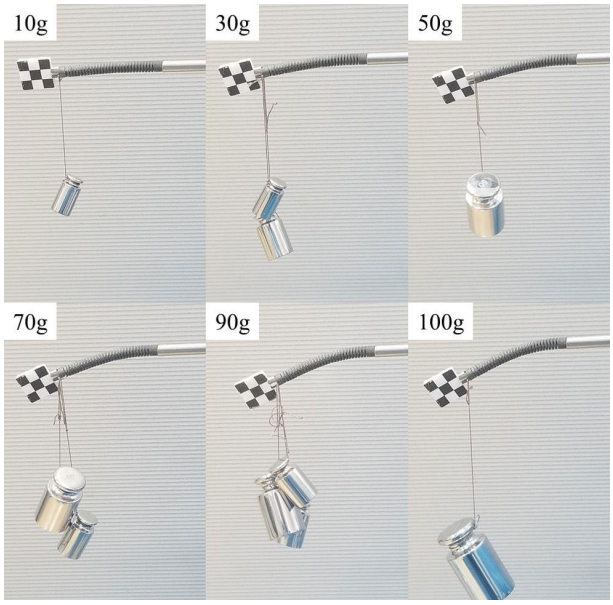

FIGURE 13. Stiffness test of a flexible joint made of 18Ni300 (heat-treated).

Comparing the stiffness test data of all the manufactured metallic flexible joints, we obtain the rule shown in Fig. 14(b),(c). It can be seen in the figures that, in general, the higher the elastic modulus of the material, the better the stiffness of the flexible joint. Specifically, under the same load, the deflection in displacement and angle are relatively less than others. We also find that there is a strong linear relationship between weight and displacement. So the linear function between them can be calculated by the least square method. But the flexible joint made of 316L steel does not conform to this rule due to its plastic deformation when the load is great. However, this result is reasonable if the force-position relationship in the plastic deformation phase [43] is taken into account. We can consider the 316L flexible joint's stiffness of the elastic deformation phase(phase1) and the plastic deformation phase(phase2) as two states. As shown in Fig. 14(a), if symbol k represent the slope of each line in Fig. 14(b), the stiffness of joints made of each material can be obtained by g/k quantitatively, where g is the gravity acceleration.

If a flexible joint with higher stiffness is used in a surgical operation, it will be less affected by external interference forces and the instruments' driving forces, but tissue damage caused by improper operation may also be greater. In connection with the above analysis results, if the maximum pulling force exerted by the pulling cables is constant, the increase in stiffness will also lead to a reduction in the workspace of the flexible joint. Therefore, after determining the type of flexible robot-assisted surgery, the operating space and safety requirements necessary for the operation should be evaluated in order to select the appropriate materials to manufacture the flexible joint.

It can be concluded from the above experiments that the TC4 titanium alloy is the best choice to manufacture the

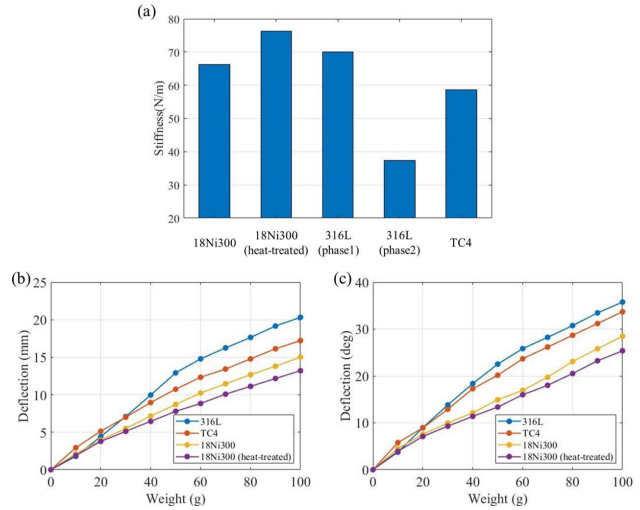

FIGURE 14. Results of the stiffness test.

flexible joints if the driven force of the instrument assembled on the distal functional part or the payload is not large. Due to its higher dexterity and less stiffness, it is safer for the contact between surgical robots and tissue. In contrast, if the instrument requires a considerable force to drive, which may influence control accuracy, the flexible joints made of 18Ni300 maraging steel(heat-treated) are recommend to reduce unexpected errors. As for surgical robots with multi-manipulators, for example, the single-port laparoscopic surgical robot which typically have one continuum manipulator for vision and two for surgical instruments [7], [8], the flexible joint for vision can be made of TC4 titanium alloy for higher dexterity, while the flexible joints for surgical instruments such as scalpel or gripper can be made of 18Ni300 maraging steel(heat-treated) for improved control accuracy. From this point of view, our approach undoubtedly provide an optimal solution compared to conventional surgical robot design scheme.

D. DESIGN VARIATIONS

In addition to the benefits mentioned above, there are more interesting research areas can be found. Some design variations that we consider valuable are listed below.

1) BENDING CHARACTERISTICS OF NON-METALLIC FLEXIBLE JOINTS

Although flexible joints made by non-metallic materials pose problems such as difficulty in accurately modeling and are greatly affected by their own and the instruments' weight, they still show excellent performance in wide-angle and small-radius bending. As shown in Fig. 15, the flexible joint made by hard rubber can still achieve a bending effect of more than 200° and a bending radius close to 9.5 mm with a cable-driven gripper. In the theoretical model and experiment, the bending radius of all metallic flexible joints is greater than 20 mm. In future work, if their mechanical characteristics are

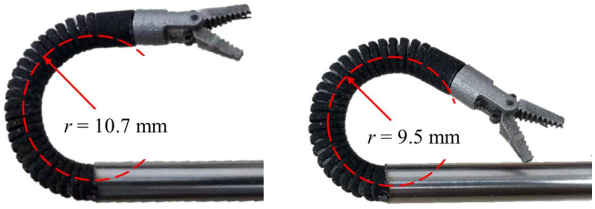

FIGURE 15. Bending condition of a flexible joint made of hard rubber.

analyzed by finite element methods or their kinematic modeling problems can be solved by machine learning methods, it is believed that such flexible joints made of non-metallic materials can offer greater advantages in the field of surgical robots.

2) PRESET STIFFNESS BY HEAT TREATMENT

From the above analysis, we can know that the presettable stiffness of the designed flexible joint is directly determined by the elastic modulus of the manufacturing material. However, in this analysis, the elastic modulus distribution of different materials is dispersed and discontinuous. Choosing the right material from the several materials used may not be to the point of a specific stiffness. At present, flexible joints manufactured using SLM technology can be heat-treated under different conditions to meet the desired elastic modulus requirements. For instance, Yin *et al.* [44] and Casati *et al.* [45] both investigated the aging behavior and the mechanical performance of selective laser-melted maraging 18Ni300 steel. Their results suggest that both the aging temperature and the aging time affect the stress-strain curves of the SLM maraging steel. From the stress-strain curves, we can see that the elasticity modulus of 18Ni300 steel is also influenced by the aging temperature and time. And it is possible to continuously control the elasticity modulus by continuous heat treatment temperature and time range. This means that it is possible to preset the stiffness of flexible joints more continuously with appropriate heat treatment.

3) MULTI-SECTION COMBINATION OF FLEXIBLE JOINTS

Fig. 16 shows the design of a 4-DOF continuum manipulator that combines two flexible joints made of different materials. The part near the functional side can be made of materials with less stiffness but higher dexterity, such as TC4 titanium alloy. The one near the control side can be made of materials with higher stiffness, such as heat-treated maraging steel 18Ni300. The advantage of this combination over the traditional multi-section with a single material is that the force coupling between the joints is reduced. As shown in Fig. 16, the tension inside the TC4 joint has a smaller effect on the deformation of the heat-treated 18Ni300 joint. Thus, it is possible not only to reduce the deformation of the heat-treated 18Ni300 joint influenced by coupling forces but also to predict the deformation using the static model presented in this paper.

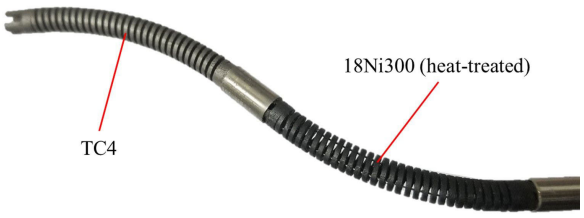

FIGURE 16. Multi-section combination of two kinds of metallic flexible joints.

In the applications of surgical robots, appropriate materials should be selected to manufacture flexible joints. For surgical robots with multi-manipulators or multi-section, combination of flexible joints made of different materials offers a more optimal solutions and better designability compared to single material one. Besides, this kind of flexible joint that can be manufactured by 3D printing not only reduces manufacturing costs and shortens the production cycle but can also be customized according to the needs of the functional instruments and the assembly requirements. There is also a purpose of this article is to provide a new method of stiffness customization for those researchers who just started their research on flexible joints or those who are not satisfied with the stiffness of well-designed flexible joints. For this paper provides a rapid remanufacturing method which is able to change the stiffness without changing the designed structure. In general, the way which stiffness can be customized during manufacturing phase tends to be ignored by researchers, so this method has not yet received much attention and may have great potential in further research.

IV. CONCLUSION

In this paper, we proposed a design of 3D-printed flexible joints for surgical robots that can be made of different materials. A kinematic model can be derived from the constant curvature assumption, and a static model can be derived from the analysis and superposition of forces. Then, a finite element analysis method is designed for the static model to obtain the correction factors, which are difficult to calculate theoretically. Furthermore, the workspaces of the joints are quantitatively analyzed three-dimensionally, and the design parameters that affect the stiffness of the flexible joints are analyzed qualitatively. We designed a static model verification system, and the results show that it achieves higher accuracy when the bending angle of the flexible joints is small. We performed a test to compare the stiffness of flexible joints made of different materials. The results reveal their different bending properties and stiffness. We also introduced some design variations, which we consider valuable for further research. Finally, the benefits of our work are summarized which indicate the great potential of those flexible joints proposed for surgical robot applications.

In future work, we will focus on a specific surgical robot system based on those flexible joints. The system may even consist of flexible joints made of different materials. The finite element analysis method also gives us some insight into the optimization of flexible joint structures. Kinematics and statics models established are valuable too. We will try to examine the effects of cable tension and friction in the flexible joint and optimize its force-position model. Based on those model, we will also attempt to design a master-slave admittance control system, which will certain improve the safety of surgical robots, rather than position control. In addition, the close-loop control and the force feedback function are also possible to be developed by using those models and the force sensing system in our validation process.

REFERENCES

[1] B. S. Peters, P. R. Armijo, C. Krause, S. A. Choudhury, and D. Oleynikov, "Review of emerging surgical robotic technology," *Surgical Endoscopy*, vol. 32, no. 4, pp. 1636–1655, Apr. 2018.
[2] C. N. Criss, M. W. Ralls, K. N. Johnson, S. Awtar, M. D. Jarboe, and J. D. Geiger, "A novel intuitively controlled articulating instrument for reoperative foregut surgery: A case report," *J. Laparoendoscopic Adv. Surgical Techn.*, vol. 27, no. 9, pp. 983–986, Sep. 2017.
[3] M. Ahmed and M. M. Billah, "Smart material-actuated flexible tendon-based snake robot," *Int. J. Adv. Robotic Syst.*, vol. 13, no. 3, p. 89, Jun. 2016.
[4] J. Y. K. Lee, B. W. O'Malley, Jr., J. G. Newman, G. S. Weinstein, B. Lega, J. Diaz, and M. S. Grady, "Transoral robotic surgery of the skull base: A cadaver and feasibility study," *ORL*, vol. 72, no. 4, pp. 181–187, 2010.
[5] W. Hong, L. Xie, J. Liu, Y. Sun, K. Li, and H. Wang, "Development of a novel continuum robotic system for maxillary sinus surgery," *IEEE/ASME Trans. Mechatronics*, vol. 23, no. 3, pp. 1226–1237, Jun. 2018.
[6] N. Simaan, K. Xu, W. Wei, A. Kapoor, P. Kazanzides, R. Taylor, and P. Flint, "Design and integration of a telerobotic system for minimally invasive surgery of the throat," *Int. J. Robot. Res.*, vol. 28, no. 9, pp. 1134–1153, Sep. 2009.
[7] K. Xu, J. Zhao, and M. Fu, "Development of the SJTU unfoldable robotic system (SURS) for single port laparoscopy," *IEEE/ASME Trans. Mechatronics*, vol. 20, no. 5, pp. 2133–2145, Oct. 2015.
[8] E. A. Arkenbout, P. W. J. Henselmans, F. Jelínek, and P. Breedveld, "A state of the art review and categorization of multi-branched instruments for NOTES and SILS," *Surgical Endoscopy*, vol. 29, no. 6, pp. 1281–1296, Jun. 2015.
[9] S. S. Jujjavarapu, A. H. Memar, M. A. Karami, and E. T. Esfahani, "Variable stiffness mechanism for suppressing unintended forces in physical human–robot interaction," *J. Mech. Robot.*, vol. 11, no. 2, pp. 1–7, Apr. 2019.
[10] M. Mahvash and P. E. Dupont, "Stiffness control of surgical continuum manipulators," *IEEE Trans. Robot.*, vol. 27, no. 2, pp. 334–345, Apr. 2011.
[11] Y.-J. Kim, S. Cheng, S. Kim, and K. Iagnemma, "A stiffness-adjustable hyperredundant manipulator using a variable neutral-line mechanism for minimally invasive surgery," *IEEE Trans. Robot.*, vol. 30, no. 2, pp. 382–395, Apr. 2014.
[12] M. Hwang, U.-J. Yang, D. Kong, D. G. Chung, J.-G. Lim, D.-H. Lee, D. H. Kim, D. Shin, T. Jang, J.-W. Kim, and D.-S. Kwon, "A single port surgical robot system with novel elbow joint mechanism for high force transmission," *Int. J. Med. Robot. Comput. Assist. Surg.*, vol. 13, no. 4, Dec. 2017, Art. no. e1808.
[13] H. M. Le, L. Cao, T. N. Do, and S. J. Phee, "Design and modelling of a variable stiffness manipulator for surgical robots," *Mechatronics*, vol. 53, pp. 109–123, Aug. 2018.
[14] Z. Li, H. Ren, P. W. Y. Chiu, R. Du, and H. Yu, "A novel constrained wire-driven flexible mechanism and its kinematic analysis," *Mechanism Mach. Theory*, vol. 95, pp. 59–75, Jan. 2016.
[15] P. Sears and P. Dupont, "A steerable needle technology using curved concentric tubes," in *Proc. IEEE/RSJ Int. Conf. Intell. Robots Syst.*, Oct. 2006, pp. 2850–2856.
[16] J. Burgner, D. C. Rucker, H. B. Gilbert, P. J. Swaney, P. T. Russell, K. D. Weaver, and R. J. Webster, "A telerobotic system for transnasal surgery," *IEEE/ASME Trans. Mechatronics*, vol. 19, no. 3, pp. 996–1006, Jun. 2014.

[17] Z. Li, L. Wu, H. Ren, and H. Yu, "Kinematic comparison of surgical tendon-driven manipulators and concentric tube manipulators," *Mechanism Mach. Theory*, vol. 107, pp. 148–165, Jan. 2017.
[18] H. M. Le, T. N. Do, and S. J. Phee, "A survey on actuators-driven surgical robots," *Sens. Actuators A, Phys.*, vol. 247, pp. 323–354, Aug. 2016.
[19] J. Burgner-Kahrs, D. C. Rucker, and H. Choset, "Continuum robots for medical applications: A survey," *IEEE Trans. Robot.*, vol. 31, no. 6, pp. 1261–1280, Dec. 2015.
[20] H.-S. Yoon and B.-J. Yi, "A 4-DOF flexible continuum robot using a spring backbone," in *Proc. Int. Conf. Mechatronics Autom.*, Aug. 2009, pp. 1249–1254.
[21] T. Kanno, D. Haraguchi, M. Yamamoto, K. Tadano, and K. Kawashima, "A forceps manipulator with flexible 4-DOF mechanism for laparoscopic surgery," *IEEE/ASME Trans. Mechatronics*, vol. 20, no. 3, pp. 1170–1178, Jun. 2015.
[22] D. Haraguchi, T. Kanno, K. Tadano, and K. Kawashima, "A pneumatically driven surgical manipulator with a flexible distal joint capable of force sensing," *IEEE/ASME Trans. Mechatronics*, vol. 20, no. 6, pp. 2950–2961, Dec. 2015.
[23] Y. Hu, L. Zhang, W. Li, and G.-Z. Yang, "Design and fabrication of a 3-D printed metallic flexible joint for snake-like surgical robot," *IEEE Robot. Autom. Lett.*, vol. 4, no. 2, pp. 1557–1563, Apr. 2019.
[24] F. Jelínek, E. A. Arkenbout, P. W. J. Henselmans, R. Pessers, and P. Breedveld, "Classification of joints used in steerable instruments for minimally invasive surgery," *J. Med. Devices*, vol. 8, no. 3, Sep. 2014, Art. no. 030914.
[25] L. Blanc, A. Delchambre, and P. Lambert, "Flexible medical devices: Review of controllable stiffness solutions," *Actuators*, vol. 6, no. 3, p. 23, 2017.
[26] M. Langer, E. Amanov, and J. Burgner-Kahrs, "Stiffening sheaths for continuum robots," *Soft Robot.*, vol. 5, no. 3, pp. 291–303, Jun. 2018.
[27] S. Zuo, K. Iijima, T. Tokumiya, and K. Masamune, "Variable stiffness outer sheath with 'dragon skin' structure and negative pneumatic shape-locking mechanism," *Int. J. Comput. Assist. Radiol. Surg.*, vol. 9, no. 5, pp. 857–865, Sep. 2014.
[28] M. Brancadoro, M. Manti, F. Grani, S. Tognarelli, A. Menciassi, and M. Cianchetti, "Toward a variable stiffness surgical manipulator based on fiber jamming transition," *Frontiers Robot. AI*, vol. 6, pp. 1–12, Mar. 2019.
[29] A. Shiva, A. Stilli, Y. Noh, A. Faragasso, I. D. Falco, G. Gerboni, M. Cianchetti, A. Menciassi, K. Althoefer, and H. A. Wurdemann, "Tendon-based stiffening for a pneumatically actuated soft manipulator," *IEEE Robot. Autom. Lett.*, vol. 1, no. 2, pp. 632–637, Jul. 2016.
[30] N. G. Cheng, M. B. Lobovsky, S. J. Keating, A. M. Setapen, K. I. Gero, A. E. Hosoi, and K. D. Iagnemma, "Design and analysis of a robust, low-cost, highly articulated manipulator enabled by jamming of granular media," in *Proc. IEEE Int. Conf. Robot. Autom.*, May 2012, pp. 4328–4333.
[31] N. Cheng, J. Amend, T. Farrell, D. Latour, C. Martinez, J. Johansson, A. McNicoll, M. Wartenberg, S. Naseef, W. Hanson, and W. Culley, "Prosthetic jamming terminal device: A case study of untethered soft robotics," *Soft Robot.*, vol. 3, no. 4, pp. 205–212, Dec. 2016.
[32] A. Gao, N. Liu, M. Shen, M. E. M. K. Abdelaziz, B. Temelkuran, and G.-Z. Yang, "Laser-profiled continuum robot with integrated tension sensing for simultaneous shape and tip force estimation," *Soft Robot.*. Accessed: Feb. 20, 2020, doi: 10.1089/soro.2019.0051.
[33] J. Back, L. Lindenroth, R. Karim, K. Althoefer, K. Rhode, and H. Liu, "New kinematic multi-section model for catheter contact force estimation and steering," in *Proc. IEEE/RSJ Int. Conf. Intell. Robots Syst. (IROS)*, Oct. 2016, pp. 2122–2127.
[34] D. Croccolo, M. De Agostinis, S. Fini, G. Olmi, A. Vranic, and S. Ciric-Kostic, "Influence of the build orientation on the fatigue strength of EOS maraging steel produced by additive metal machine," *Fatigue Fract. Eng. Mater. Struct.*, vol. 39, no. 5, pp. 637–647, May 2016.
[35] A. Hadi, M. Qasemi, M. Elahinia, and N. S. Moghaddam, "Modeling and experiment of a flexible module actuated by shape memory alloy wire," in *Proc. ASME Conf. Smart Mater., Adapt. Struct. Intell. Syst. Amer. Soc. Mech. Eng. Digit. Collection*, Sep. 2014, pp. 1–10.
[36] J. U. Franc, P. Nováčková, and P. Janíček, "Torsion of a non-circular bar," *Eng. Mech.*, vol. 19, no. 6, pp. 45–60, 2012.
[37] W. C. Young and R. G. Budynas, "Properties of a plane area," in *Roark's Formulas for Stress and Strain*, 7th ed. New York, NY, USA: McGraw-Hill, 2002, pp. 401–808.
[38] Y. Z. Chen, "Torsion problem of rectangular cross section bar with inner crack," *Comput. Methods Appl. Mech. Eng.*, vol. 162, nos. 1–4, pp. 107–111, Aug. 1998.
[39] B. Richard and N. Keith, "Mechanical springs," in *Shigley's Mechanical Engineering Design*, 9th ed. New York, NY, USA: McGraw-Hill, 2011, pp. 519–521.
[40] G. Shanmugasundar, R. Sivaramakrishnan, S. Meganathan, and S. Balasubramani, "Structural optimization of an five degrees of freedom (T-3R-T) robot manipultor using finite element analysis," *Mater. Today, Proc.*, vol. 16, pp. 1325–1332, 2019.
[41] Y. Elsayed, A. Vincensi, C. Lekakou, T. Geng, C. M. Saaj, T. Ranzani, M. Cianchetti, and A. Menciassi, "Finite element analysis and design optimization of a pneumatically actuating silicone module for robotic surgery applications," *Soft Robot.*, vol. 1, no. 4, pp. 255–262, Dec. 2014.
[42] P. Corke, *Robotics Vision and Control: Fundamental Algorithms in MATLAB*. Berlin, Germany: Springer, 2013.
[43] T. M. Mower and M. J. Long, "Mechanical behavior of additive manufactured, powder-bed laser-fused materials," *Mater. Sci. Eng., A*, vol. 651, pp. 198–213, Jan. 2016.
[44] S. Yin, C. Chen, X. Yan, X. Feng, R. Jenkins, P. O'Reilly, M. Liu, H. Li, and R. Lupoi, "The influence of aging temperature and aging time on the mechanical and tribological properties of selective laser melted maraging 18Ni-300 steel," *Additive Manuf.*, vol. 22, pp. 592–600, Aug. 2018.
[45] R. Casati, J. Lemke, A. Tuissi, and M. Vedani, "Aging behaviour and mechanical performance of 18-Ni 300 steel processed by selective laser melting," *Metals*, vol. 6, no. 9, p. 218, Sep. 2016.

FAN FENG received the B.Eng. degree in material forming and control engineering from the Harbin Institute of Technology, Harbin, China, in 2017. He is currently pursuing the Ph.D. degree in materials science and engineering with Shanghai Jiao Tong University, Shanghai, China.

His research interests include continuum robots and robot control.

WUZHOU HONG received the B.Eng. degree in material forming and control engineering from Chongqing University, Chongqing, China, in 2015. He is currently pursuing the Ph.D. degree in materials science and engineering with Shanghai Jiao Tong University, Shanghai, China.

His research interests include surgical robots and continuum robots.

LE XIE (Member, IEEE) received the B.Sc. degree in mathematics from East China Normal University, Shanghai, China, in 1985, and the M.S. degree in computing mathematics and the Ph.D. degree in manufacture of aeronautics and astronautics from the Nanjing University of Aeronautics and Astronautics, Nanjing, China, in 1995 and 1999, respectively.

He is currently a Professor with the National Engineering Research Center of Die and Mold CAD, Shanghai Jiao Tong University, Shanghai. His research interests include surgical robots and rehabilitation robots.